ACS OMEGA

Article

Cite This: ACS Omega 2019, 4, 18289−18298

http://pubs.acs.org/journal/acsodf

# Optimization of the Synthesis of Copper Ferrite Nanoparticles by a Polymer-Assisted Sol−Gel Method

Jaume Calvo-de la Rosa and Mercè Segarra*

DIOPMA Centre, Department of Materials Science and Physical Chemistry, Faculty of Chemistry, IN2UB, Universitat de Barcelona, Martí i Franquès 1, 08028 Barcelona, Spain

**ABSTRACT:** Magnetic ferrites are used in a wide range of technological applications, such as biomedicine, electronics, or energy. They also present interesting magnetic properties, especially for high-frequency applications. These materials have been prepared by a large variety of methods, from basic solid-state reaction to advanced wet chemical methods. However, most of these approaches are complex and have low production rates. In this work, a deep analysis of an easy polymer-assisted sol−gel synthesis of copper ferrite ($CuFe_2O_4$) nanoparticles is done. A multivariate analysis, by means of the design of experiments approach, is carried out to account for two variables at a time. Moreover, a wide experimental domain is explored, and the impact of each variable on the chemical composition and magnetic properties is determined. This work results in an optimization of the synthesis method to obtain high-purity nanoparticles (∼96%).

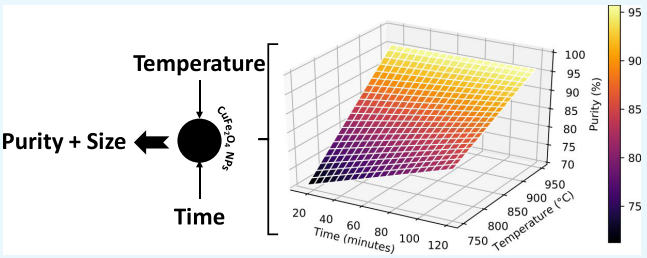


## INTRODUCTION

Magnetic materials are a family of materials widely used in technological applications. The changes in properties that they experiment when their size is reduced to the nanometric scale make them even more interesting than those in the bulk form. They have been claimed as promising candidates for medical diagnostics[1] and treatment,[2−4] sensors,[5] improving the efficiency and opening new opportunities in the energy sector,[6,7] and data storage[8,9] for instance.

Spinel ferrites have a structure with the form $MFe_2O_4$, where M is a divalent cation and typically a transition metal. Oxygen ($O^{2-}$) ions form a face-centered cubic structure, $Fe^{3+}$ cations occupy half of the octahedral holes ($h_O$), and $M^{2+}$ ions are placed in eight of the tetrahedral holes ($h_T$). In particular, copper ferrite ($CuFe_2O_4$) has an inverse spinel structure, which has a different occupation of the vacancies: $M^{2+}$ cations are placed in $h_O$ with half of the $Fe^{3+}$ ions, whereas the other half are in $h_T$.

These types of materials have been previously prepared by a wide range of wet synthesis methods, such as co-precipitation,[10−12] thermal decomposition,[13,14] sonochemical,[15−18] or solvothermal.[19,20] Most of these methods ensure good results in terms of low particle size and morphology control, but, on the other hand, it is usually complex to have a precise control over the process, and the production rate is low. On the other hand, high-temperature solid-state methods are simple and easy to scale up. However, the degree of control that they have over the properties of the final material is poor. In this scenario, the sol−gel and gel combustion technique[21−26] appears as a promising option due to its simplicity and control over the product characteristics. For this reason, different researchers have recently used this method in their work. For instance, López-Ramón et al.[22] and Zhuravlev et al.[23] showed the formation of both phases, tetragonal and cubic, depending on the synthesis conditions. The report from Masunga et al.[27] is a good summary of the work previously done in this field.

Although there is an extensive list of interesting publications regarding the sol−gel preparation of $CuFe_2O_4$, there is a lack of a deep analysis of the process under a wide range of conditions. Previous papers tend to work under specific conditions, or only one variable is modified when its effect is explored. In this work, we provide a multivariable analysis, by means of the design of experiments (DoE) approach,[28] to numerically quantify the effect of the calcination time and temperature. Thus, our work explores two variables at a time and accounts for their possible interaction. Moreover, two analysis cycles are performed to explore a wider experimental domain. The effect that each variable has on the chemical composition and magnetic properties is determined. This work leads to an optimization of the polymer-assisted sol−gel synthesis[29] of $CuFe_2O_4$ nanoparticles to maximize the product purity.

## RESULTS AND DISCUSSION

Based on the obtained results from preliminary experiments, the conditions chosen for the first DoE are presented in Table 1. The temperature limits have been set to 750 and 950 °C, whereas the time varies from 15 min to 2 h.

This first batch of samples has been characterized by X-ray diffraction (XRD) to determine their crystal structure and

Received: July 23, 2019
Accepted: September 16, 2019
Published: October 21, 2019






DOI: 10.1021/acsomega.9b02295
ACS Omega 2019, 4, 18289−18298

**Table 1. Experimental Matrix for the First DoE Cycle**

| experiment # | time level (min) | temperature level (°C) |
|---|---|---|
| 1 | 15 | 750 |
| 2 | 120 | 750 |
| 3 | 15 | 950 |
| 4 | 120 | 950 |

chemical composition. Figure 1 shows a general comparison of the four obtained patterns.

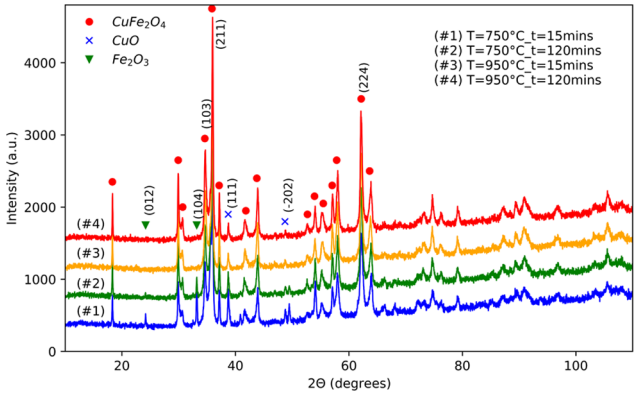


**Figure 1.** XRD patterns of the four samples prepared in the first batch of experiments. All of the patterns have been spaced 400 units to facilitate their visualization and comparison. The different markers indicate the $2\theta$ positions of the main peaks of the three phases.

By analyzing these results, it is possible to corroborate that the desired $CuFe_2O_4$ phase is predominant in all of the experiments. It has a tetragonal structure with cell parameters of $a = b = 5.8444$ Å and $c = 8.6340$ Å. Moreover, smaller quantities of rhombohedral $Fe_2O_3$ and monoclinic CuO are also detected. The presence of these structures is in good agreement with the obtained results under similar conditions by other authors.[22] The characteristic $CuFe_2O_4$ peak at around 18° is present in all of the samples, but it seems clear that the peak at 24°, which corresponds to $Fe_2O_3$, disappears as the thermal treatment becomes more intense (larger times and higher temperatures). Therefore, it is seen that higher temperatures and longer times favor the ferrite formation, as could be expected. Considering that the relative peak intensity is directly proportional to the presence of each phase, and that all of the samples have been consecutively measured in the same device and under the same conditions, it is possible to make a first approximation to determine their relative purity. Figure 2 zooms different peaks from Figure 1 to make a clearer comparison.

In Figure 2A,B, the presence of $CuFe_2O_4$ is evident as the temperature and time increase. Samples are perfectly ordered according to their calcination conditions: in both cases, sample #1 (15 min at 750 °C) is the one with a lower intensity (around 30% less than the higher peak), whereas sample #4 (120 min at 950 °C) shows the maximum intensity. Meanwhile, samples #2 and #3 present intermediate behaviors. Nevertheless, the relative intensity of the sample at 950 °C is higher than that of the one at 750 °C even though the calcination time is longer in the second case. This means that, in this range, temperature seems to have a major impact on the chemical composition than time, i.e., high-purity products can be obtained in fast reactions at high temperatures. According to the conclusions obtained by Khemthong et al.,[30] $CuFe_2O_4$ is mainly formed during the gel combustion, whereas the later calcination processes determine the crystallinity and phase purity. The observed tendency perfectly supports what is expected from a thermodynamic point of view: the chemical reaction between CuO and $Fe_2O_3$ is favored for higher-energy inputs.

Even though this first analysis seems to clearly show that the phases are formed, all of the samples have been analyzed by the Rietveld refinement[31] to extract quantitative information about their chemical composition. In Figure 3, the result of the refinement for one of the samples is shown.

As can be observed, the relative intensity between peaks of the same phase is not accurate. This might be due to the presence of a preferred crystallographic orientation (which is unexpected in powder samples) or because the considered structural model for the calculation is not fully strict with the

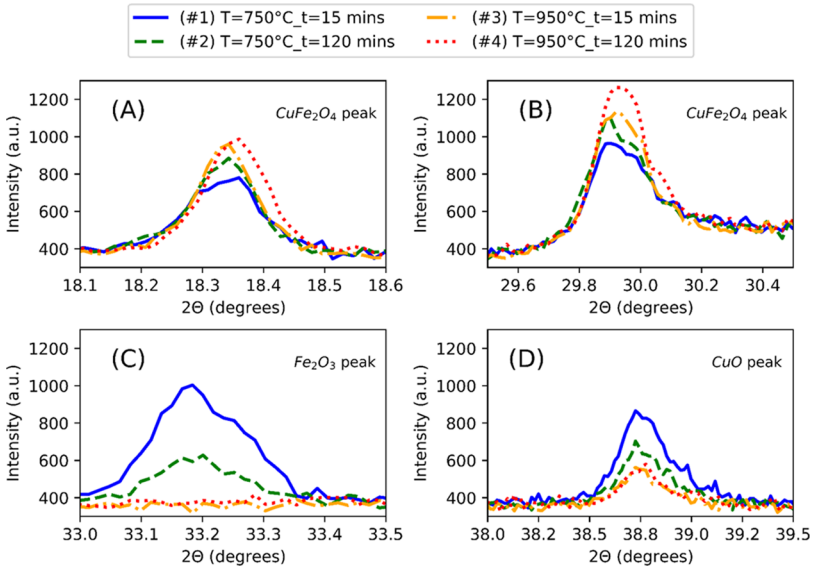


**Figure 2.** Zoomed peaks of the first batch of samples. (A) and (B) are $CuFe_2O_4$ peaks, (C) is a $Fe_2O_3$ peak, and (D) is a CuO peak.



DOI: 10.1021/acsomega.9b02295
ACS Omega 2019, 4, 18289−18298

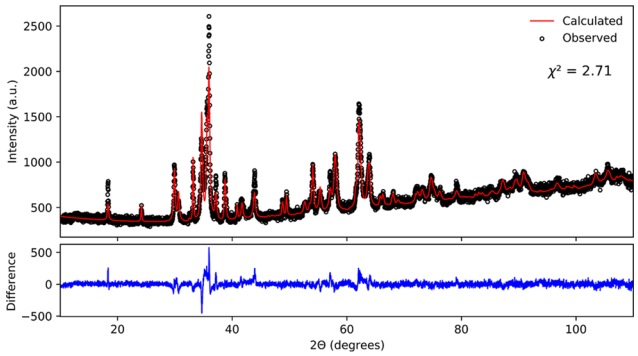


**Figure 3.** Rietveld refinement of sample #1 from the first batch of samples. Measured data is represented by circles, whereas the continuous red line shows the calculated model. The difference between both values is represented in the bottom plot.

reality. Nevertheless, as the scale factor, peak shape, and unit cell parameters are correctly adjusted, the results are rigorous with the purity of each sample. The average crystallite size, determined by the Scherrer formula, is 13.46 nm, confirming thus the nanometric structure of the material. A resume of the obtained compositions is presented in Table 2.

**Table 2. Rietveld Refinement Compositions Obtained for the First Batch of Samples**[a]

| sample (#) | $CuFe_2O_4$ (%) | CuO (%) | $Fe_2O_3$ (%) | $\chi^2$ |
|---|---|---|---|---|
| 1 | 70.3 | 8.4 | 21.3 | 2.71 |
| 2 | 83.2 | 5.7 | 11.1 | 2.86 |
| 3 | 95.6 | 4.4 | 0.0 | 3.02 |
| 4 | 95.7 | 4.0 | 0.3 | 3.02 |

[a] $\chi^2$ represents the quality of the adjustment.

Again, the formation of $CuFe_2O_4$ and the consumption of CuO and $Fe_2O_3$ at high temperatures and long times are confirmed, as could be expected from a thermodynamic point of view.

Once the percentage of $CuFe_2O_4$ is obtained from each experiment, it is possible to calculate the values of all of the parameters in eq 1. The obtained values are $b_0$ = 86.2, $b_1$ = 3.3, $b_2$ = 9.5, and $b_{12}$ = −3.2. Then, we have predicted the purity ($Y$) at any point in the area between the tested experimental points. Figure 4 graphically represents the obtained coefficients, as well as the calculated $Y$ values in all of the experimental domain.

By analyzing the coefficients, it is possible to extract two main conclusions: (i) the calcination temperature ($b_2$) has approximately three times the impact on the chemical composition than the time ($b_1$), as it was predicted by analyzing the XRD pattern in Figure 2; (ii) the magnitude of the interaction variable ($b_{12}$) is on the order of magnitude of $b_1$, so, apart from the individual effects, there is a considerable interaction between both variables.

To study the effect that these variables have on the particle size, Figure 5 shows the number and volume particle size distributions for each sample.

In all samples, most of the particles are in the nanometric range because the number distribution is centered under 100 nm. On the other hand, the major part of the volume of the sample is occupied by micrometer-sized particles. This double effect can be due to two different factors: (i) most of the particles are nanometric in size, but there are others (much lower in number) that are orders of magnitude bigger and have a greater influence when representing the volume fraction (it would happen in a synthesis process with an extremely low degree of control); (ii) nanoparticles have been formed, but then they get attached to each other by thermal processes (i.e., sintering) forming micrometric clusters. The shape of the volume distribution suggests that different distributions coexist in the sample. Therefore, the formation of clusters may be the origin of these micrometric bodies. Otherwise, a more continuous distribution should be expected if micrometric particles would have been formed. Moreover, as LD principles assume spherical particles, the different superposed peaks could also be originated by irregular-shaped particles, which is common in aggregates.

The physical aspect of particles has been checked by SEM to have a clear idea about their morphology. Figure 6 shows some of the images of these samples.

In the four cases, it can be seen how micrometric clusters are formed by the agglomeration of submicrometric particles. These results verify the arguments presented from the LD results. Also, the size distribution of aggregates is wide and the shape is irregular in all samples, in good agreement with the volume LD results.

Now, it is clear that small particles have been synthesized, but due to the calcination effect, they behave as building blocks that sinter each other, forming bigger agglomerates. The size of the individual small particles is difficult to be determined with these images, but it is clear that their size is below 1 $\mu$m. Furthermore, by looking below the big aggregates, it is possible to find a distribution of particles that are smaller in size than those particles forming the agglomerates. This smaller

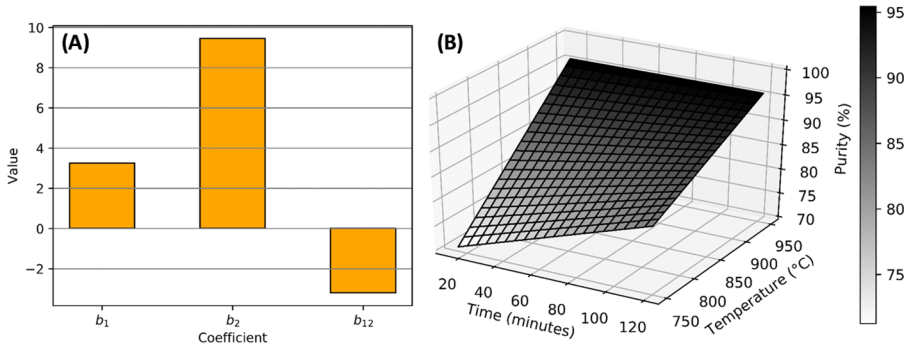


**Figure 4.** (A) Obtained parameters for $b_1$, $b_2$, and $b_{12}$; (B) first DoE-calculated purity values.



DOI: 10.1021/acsomega.9b02295
ACS Omega 2019, 4, 18289−18298

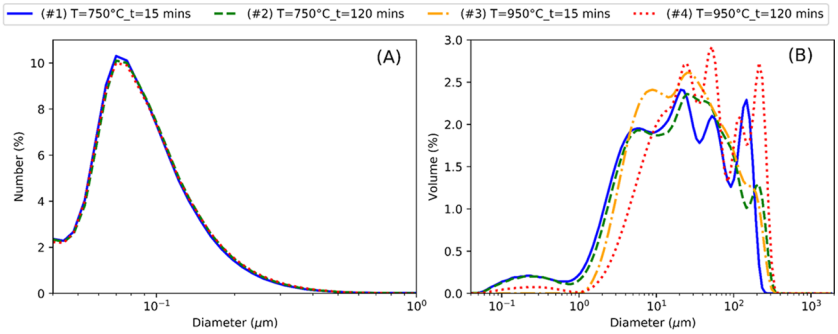


**Figure 5.** Particle size distribution of the first batch of samples represented as a function of (A) number of particles and (B) volume fraction.

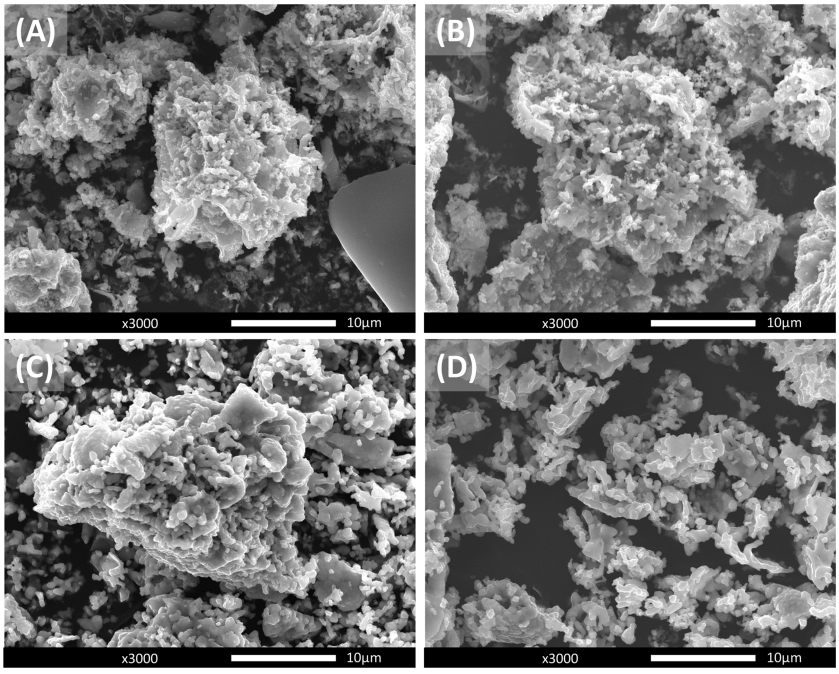


**Figure 6.** SEM images at ×3000 magnification of all of the powder samples from the first batch: (A) sample #1, (B) sample #2, (C) sample #3, and (D) sample #4.

distribution, which is considerably below 1 $\mu$m in diameter, may be a representative of those nanometric particles that have not sintered with others, keeping in this way their original size. Even though the shape of the aggregates is irregular, individual nanoparticles seem to be spherical shaped.

All of these results are in good agreement with those from the LD particle size analysis and have been already observed in above-mentioned works.[13,15,22,23] Therefore, number percentage distributions can be understood as a representation of the size of the formed particles, whereas the volume percentage distribution gives information about the sintering process between the previously formed nanoparticles.

Once the real meaning of each representation has been discussed, it is time to come back to Figure 5. In the number percentage representation, there is almost no difference between the size distribution of the nanoparticles prepared at different conditions. The resolution of the measurement is bigger than the difference produced for the different conditions. The mean value of these distributions is 93.3 ± 0.7 nm. This result, together with the previous Scherrer calculation, suggests the formation of a polycrystalline microstructure, as the mean particle size is greater than the mean crystallite size. On the other hand, by studying the volume percentage distributions, it is clear how the distribution is progressively shifted to bigger diameters as the calcination intensifies. Even though it consists of the superposition of different peaks, the main distribution has a clear dependence on the thermal treatment. Consequently, the effect that the thermal treatment has on sintering between particles is demonstrated.

Overall, the inverse effect that these conditions have on the final goal of this work can be seen: when the calcination is more intense, purity and sintering between particles increase; for soft calcinations, the sintering is lower and the product is less pure. Thus, an optimum balance between both variables needs to be found to have high-purity products and, at the same time, reduce as much as possible the sintering between nanoparticles.

Finally, the magnetic hysteresis cycle [M(H)] of these samples has been measured. As can be observed in Figure 7, only the first magnetization curve and the demagnetization from the positive to the negative saturations have been measured. As the hysteresis cycle has a symmetric behavior when the magnetic field is reversed, these conditions are sufficient for measuring the properties under study in this work.



DOI: 10.1021/acsomega.9b02295
ACS Omega 2019, 4, 18289−18298

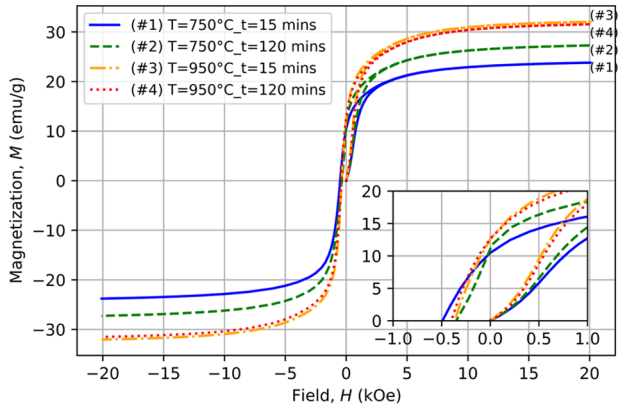


**Figure 7.** SQUID M(H) measurements for the first batch of samples. The inner plot is a zoomed representation of the data close to the origin of coordinates.

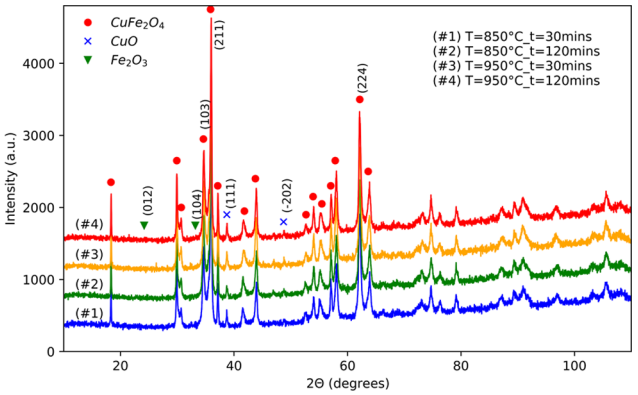


**Figure 8.** XRD patterns of the four samples prepared in the second batch of experiments. All of the patterns have been spaced 400 units to facilitate their visualization and comparison. The different markers indicate the $2\theta$ positions of the main peaks of the three phases.

These results clearly show how the saturation magnetization ($M_S$), i.e., the maximum magnetization that can be achieved by the material, increases as the thermal treatment becomes stronger. Also, by examining the inner plot, it is seen how the magnetic permeability ($\mu$, which corresponds to the slope of the first magnetization curve) is also dependent on the thermal treatment. For both commented magnetic properties, when the sample is prepared at 750 °C, there is a strong dependence on the treatment time, whereas it is weaker or inexistent when the sample is prepared at 950 °C. Additionally, the remanent magnetization ($M_R$) and the coercive field ($H_C$) have the same increasing tendency at stronger calcination conditions, except in the case of sample #1. All of the quantitative results are summarized in Table 3. The tendency in all cases follows the compositional results determined by XRD, having higher $M_S$, $M_R$, $H_C$, and $\mu$ than those samples with a higher $CuFe_2O_4$ content.

**Table 3. Magnetic Properties of the First Batch of Samples**

| sample (#) | $M_S$ (emu/g) | $M_R$ (emu/g) | $\lvert H_C \rvert$ (Oe) |
|---|---|---|---|
| 1 | 23.7 | 10.5 | 491.3 |
| 2 | 27.2 | 11.1 | 349.6 |
| 3 | 31.9 | 12.6 | 365.8 |
| 4 | 31.4 | 12.7 | 400.3 |

Once the first conditions were tested, this work focused its attention on a more detailed study of a smaller region around the optimum (previously represented in Figure 4B). By considering that there are no significant differences in the size of the formed nanoparticles, the region where higher purities have been achieved is zoomed. The new conditions are described inTable 4. XRD results of this second batch of samples are shown in Figure 8.

All of the analyzed samples have the same predominant crystalline $CuFe_2O_4$ phase found in the first batch, with smaller traces of CuO and $Fe_2O_3$. It is worth noticing that the characteristic peaks of these undesired phases have been considerably reduced and are difficult to be detected with this view. Again, to make a better comparison between the different synthesis conditions, some peaks are zoomed and shown in Figure 9. The selected peaks are the same as those in Figure 1.

**Table 4. Experimental Matrix for the Second DoE Cycle**

| experiment # | time level (min) | temperature level (°C) |
|---|---|---|
| 1 | 30 | 850 |
| 2 | 120 | 850 |
| 3 | 30 | 950 |
| 4 | 120 | 950 |

In Figure 9A,B, two $CuFe_2O_4$ peaks are represented. It can be seen that, despite the case of sample #1, all of the samples are close to the maximum value. In addition, sample #2 is slightly less intense, and those samples prepared at 950 °C reach the same values independently of the calcination time. Figure 9C,D represents impurity peaks. The first, corresponding to a characteristic $Fe_2O_3$ peak, is actually inexistent for the four samples, giving thus a good idea about the purity improvement in this batch. Finally, the last image indicates that all samples still have some CuO traces, which are almost the same in all of them. To have more detailed information, all samples have been refined by the Rietveld method. Figure 10 shows the profile fitting done for one of the samples, and Table 5 contains the refined values.

The Rietveld refinement confirms what was suggested before: the purity is excellent in all of the samples and all of the values are extremely similar. The small diversity is not significant and is influenced by the small differences in the profile fitting quality. The mean purity value is 95.8 ± 0.2%. This similarity in the results suggests that in these conditions a maximum purity is reached.

When these experimental responses are used to deduce the model described in eq 1, the parameters obtained are $b_0 = 95.8$, $b_1 = 0.1$, $b_2 = -0.1$, and $b_{12} = 0.0$. The graphical representation of these values and the predicted purity are represented in Figure 11.

In this second design of samples, the obtained coefficients are substantially lower than those obtained in the first design. In contrast with the first batch, now the relative value of $b_{12}$ is much lower than $b_1$ and $b_2$. These results are consistent with the fact that the chemical composition is almost constant in this range. Moreover, the surface represented in Figure 11B is almost constant in all of the experimental domain. Even though it may seem that there is some slope, the corresponding small purity should be taken into account. Finally, to check the model results obtained here, an extra sample with intermediate conditions has been prepared and characterized. This sample has been prepared at 900 °C for 60 min, and the



DOI: 10.1021/acsomega.9b02295
ACS Omega 2019, 4, 18289−18298

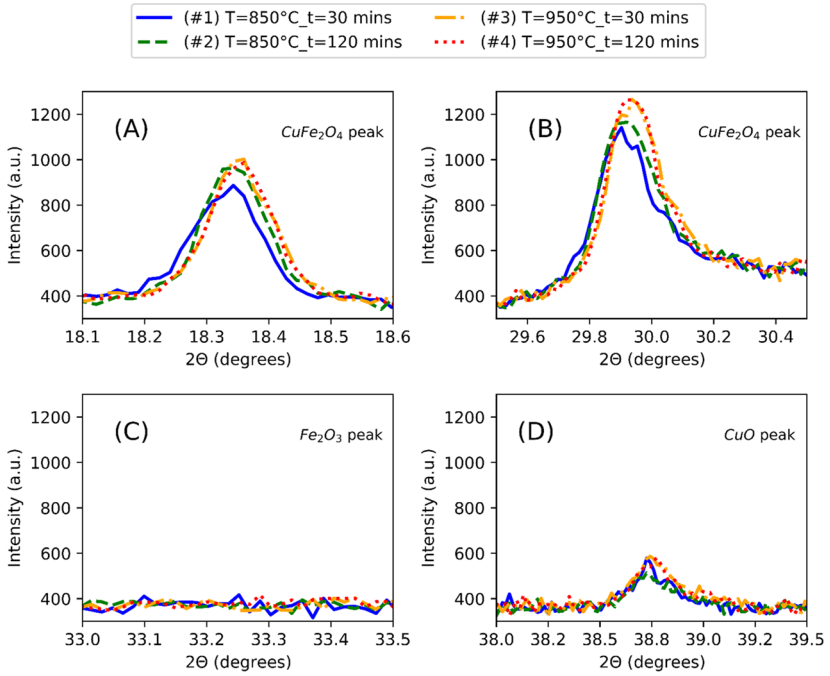


**Figure 9.** Zoomed peaks of the second batch of samples. (A) and (B) are $CuFe_2O_4$ peaks, (C) is a $Fe_2O_3$ peak, and (D) is a CuO peak.

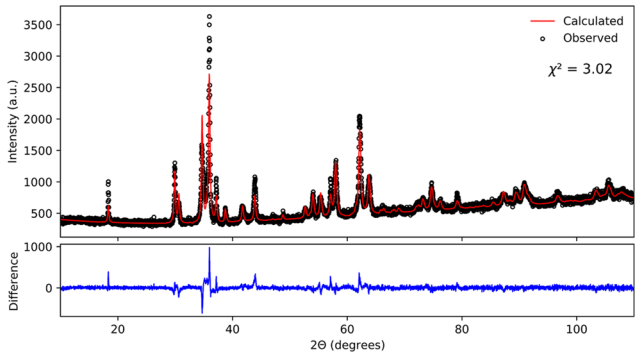


**Figure 10.** Rietveld refinement of sample #4 from the second batch of samples. Measured data is represented by circles, whereas the continuous red line shows the calculated model. The difference between both values is represented in the bottom plot.

**Table 5. Rietveld Refinement Compositions Obtained for the Second Batch of Samples**[a]

| sample (#) | $CuFe_2O_4$ (%) | CuO (%) | $Fe_2O_3$ (%) | $\chi^2$ |
|---|---|---|---|---|
| 1 | 95.8 | 3.9 | 0.3 | 3.19 |
| 2 | 96.1 | 3.5 | 0.4 | 3.18 |
| 3 | 95.6 | 4.2 | 0.2 | 3.26 |
| 4 | 95.7 | 4.0 | 0.3 | 3.02 |

[a] $\chi^2$ represents the quality of the adjustment.

corresponding purity obtained by the Rietveld refinement is 95.7% with $\chi^2$ = 3.08. This chemical composition is consistent with the predicted values under the same conditions (95.8%), and, hence, the model is validated.

These stable composition values are similar to those obtained in other works, which synthesize $CuFe_2O_4$ nanoparticles by similar methods.[22,23,32] Even though the maximum reported purities in these works (95%) are slightly lower than ours, it is worth mentioning that these studies used maximum calcination temperatures of 800 °C, whereas our second batch is prepared at a calcination temperature of 850 °C. As it has been clearly demonstrated in this study, this difference in temperature can lead to an increase of ferrite conversion. On the other hand, all works agree on the formation of the tetragonal phase of $CuFe_2O_4$ in the studied temperature range.

This second batch of samples has also been analyzed by LD to study their particle size distribution. Results are shown in Figure 12.

Again, all samples have their number percentage distribution centered under 100 nm, certifying their nanometric nature. No clear differences are detected between samples, which have a mean value of 93.1 ± 1.4 nm. These results are on the same order as those obtained for the first batch. Regarding the volume percentage distribution, a curious behavior is seen: those samples calcinated at lower temperatures (#1, #2) are displaced to bigger sizes. On the other hand, the aspect of patterns suggests that the distributions are more homogeneous when the sample is processed at lower temperatures, which corresponds to a lower degree of particle sintering and agglomeration.

The behavior seen in Figure 13 is similar to the one previously discussed in Figure 6: spherical-shaped nanometric particles sinter by thermal processes, forming micrometric clusters. Nanoparticles have been clearly formed, but the applied thermal energy produces this sintering effect between particles. Therefore, an equilibrium needs to be found to maximize the ferrite purity and to avoid sintering. Once the maximum purity is reached, as happens in this second batch, it is recommended to work at the lower possible temperature and time to reduce the agglomeration.

These final samples have also been analyzed by SQUID magnetometry. The hysteresis cycle results are shown in Figure 14.

As could be expected from the chemical and crystallographic results, here, the magnetic behavior is much more similar between samples than in the first batch. Nevertheless, there is still a small difference in $M_S$ and $\mu$ between those samples



DOI: 10.1021/acsomega.9b02295
ACS Omega 2019, 4, 18289−18298

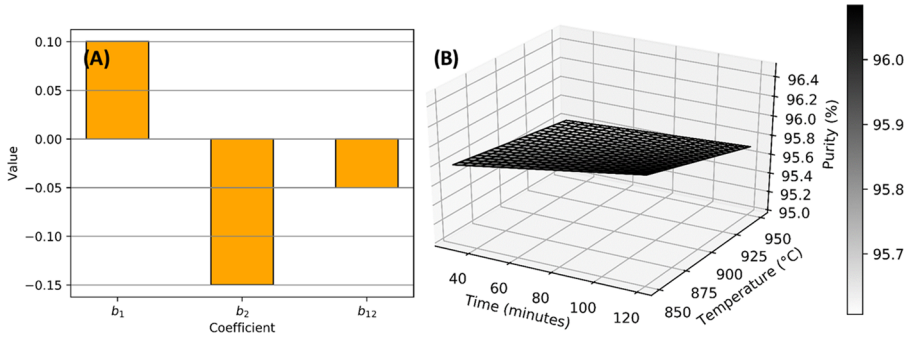


**Figure 11.** (A) Obtained parameters for $b_1$, $b_2$, and $b_{12}$; (B) second DoE-calculated purity values.

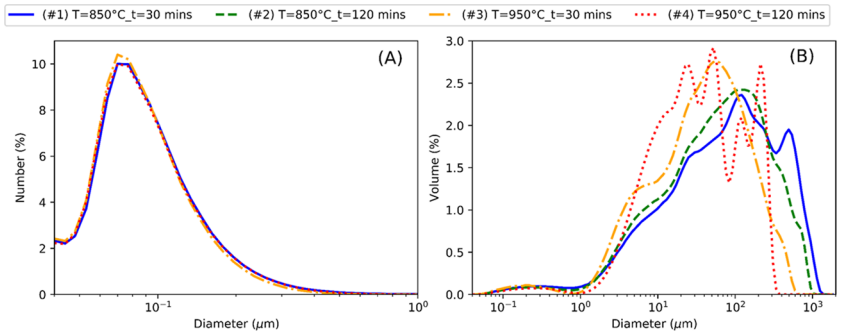


**Figure 12.** Particle size distribution of the second batch of samples represented as a (A) function of the number of particles and (B) as the percentage of volume that each diameter represents in the hole sample.

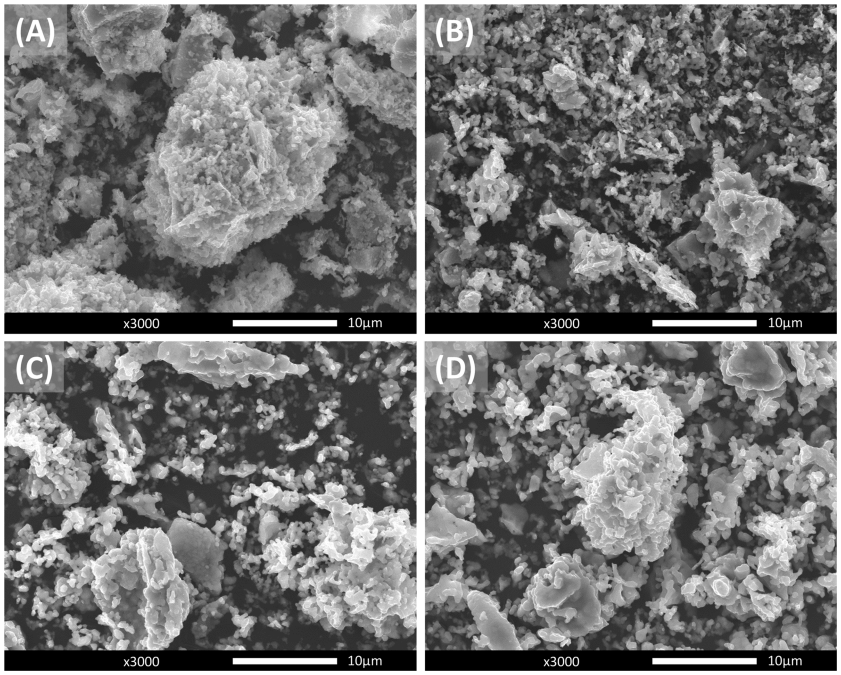


**Figure 13.** SEM images at ×3000 magnifications of all of the powder samples of the second batch: (A) sample #1, (B) sample #2, (C) sample #3, and (D) sample #4.

prepared at 850 and 950 °C, where they are higher when the calcination is more intense. Although the differences are now smaller, it is possible to see how those samples prepared at higher temperatures have smaller values of $M_R$ and $H_C$. It is contrary to what has been obtained for the first batch of samples. Nevertheless, it should be considered that the differences in these cases are much smaller and they may be in the error range of the measurement. Finally, the main parameters obtained from these measurements are shown in Table 6.

The obtained $M_S$ values are greater than those previously reported for $CuFe_2O_4$ nanoparticles prepared by similar methods,[22,32,33] which show values between 20 and 28 emu/g. In samples treated at 800 °C, López-Ramón et al. reported much softer magnetic properties, with approximately $M_R$ values of 0.8 emu/g and $H_C$ of 30 Oe. Anandan et al. obtained similar



DOI: 10.1021/acsomega.9b02295
ACS Omega 2019, 4, 18289−18298

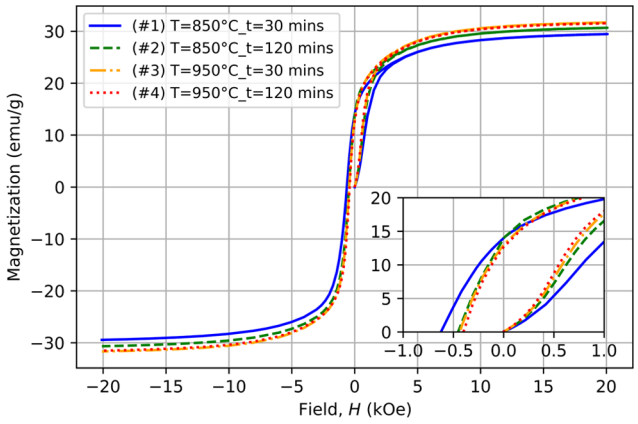


**Figure 14.** SQUID M(H) measurements for the second batch of samples. The inner plot is a zoomed representation of the data close to the origin of coordinates.

**Table 6. Magnetic Properties of the Second Batch of Samples**

| sample (#) | $M_S$ (emu/g) | $M_R$ (emu/g) | $\|H_C\|$ (Oe) |
|---|---|---|---|
| 1 | 29.3 | 14.0 | 623.6 |
| 2 | 30.6 | 13.9 | 453.4 |
| 3 | 31.7 | 13.0 | 437.1 |
| 4 | 31.4 | 12.7 | 400.3 |

remanence and coercivity values ($M_R$ of 12 emu/g and $H_C$ of 631 Oe), whereas Sumangala et al. results show a harder behavior ($H_C$ of around 1 kOe). The paper published by Yadav et al.[34] reports values of $M_S$ = 25 emu/g, $M_R$ = 8, and $H_C$ = 218 Oe when the tetragonal phase is completely formed. These results are on the same order of magnitude as ours but with a softer behavior.

Table 7 provides an overall comparison of our results with those previously reported by other authors. The sample prepared at 850 °C has been used for the comparison because its conditions are similar to those in other studies and it may be considered to represent the optimal conditions found in the second DoE. Only studies with the same crystal structure have been considered for a more rigorous comparison.

It is appreciable that both the purity and $M_S$ values reported in our work are greater than the values of all of these papers using similar synthesis methods and forming the tetragonal crystal structure. The elevated $M_S$ level achieved in this work may be a consequence of the high sample purity, according to the tendencies observed in the first DoE. Moreover, it is possible to see that we are even obtaining better results than other works carrying out the calcination at higher temperatures. Furthermore, our calcination process is clearly faster than the others, confirming the low impact of the time on the obtained properties. Therefore, the hypothesis stating that short calcinations at high temperatures are probably the best option is reinforced.

The dependence of $M_S$ and $M_R$ on the $CuFe_2O_4$ content is shown in Figure 15. All of the samples from both batches have been represented. As can be clearly seen, both magnitudes increase with the $CuFe_2O_4$ content. For high-purity samples, the values are almost constant, which can be assumed as those corresponding to the pure $CuFe_2O_4$. Overall, the formation of the complex ferrite from its former oxides increases the saturation magnetization, although it is accompanied by a slight increase of the remanence.

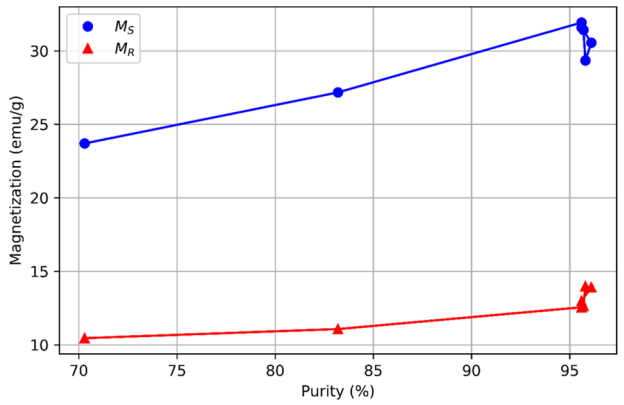


**Figure 15.** Saturation magnetization ($M_S$) and remanent magnetization ($M_R$) dependence on the simple purity.

## CONCLUSIONS

In this work, copper ferrite nanoparticles have been successfully synthesized by means of a simple polymer-assisted sol−gel method. The process and the conditions have been described, and the process has been studied in a wide range of conditions. A multivariate analysis, by means of the design of experiments approach, has allowed us to do a multivariable analysis of the effect of the calcination time and temperature on the nanoparticle properties. Furthermore, it has been proved a higher agglomeration of particles for stronger calcinations.

The first DoE planned in a wide range of conditions has been useful to confirm that the ferrite conversion improves for calcinations at high temperatures and long times. Moreover, temperature has been observed to have a stronger impact on the final properties than time. The second DoE has shown a plateau on chemical composition and magnetic properties above 850 °C. Therefore, the optimum conditions have been set to calcination at 850 °C for 30 min.

**Table 7. Comparison of the Results Obtained in This Work with the Literature[a]**

| references | calcination temperature (°C) | calcination time (min) | spinel crystal structure | purity (%) | $M_S$ (emu/g) |
|---|---|---|---|---|---|
| this work | 850 | 30 | tetragonal | 96 | 31 |
| López-Ramon[22] | 800 | 180 | tetragonal | 88 | 25 |
| Zhuravlev[23] | 800 | 240 | tetragonal | 95 | – |
| Sumangala[32] | 800 | – | tetragonal | 95 | 28 |
| Anandan[33] | 900 | 180 | tetragonal | – | 21 |
| Yadav[34] | 1100 | 120 | tetragonal | – | 25 |

[a]"–" symbol indicates unknown information.



DOI: 10.1021/acsomega.9b02295
ACS Omega 2019, 4, 18289−18298

The results obtained in this work are an improvement over those previously published by other authors in similar conditions. The sample purity (96%), as well as the saturation magnetization (31 emu/g), is slightly higher than that found by other authors. However, we have not been able to obtain perfectly isolated nanoparticles, as they sinter during calcination. Moreover, the number distribution of the nanoparticles could not be obtained in detail for each sample due to resolution limitations.

Future work should be addressed to the reduction of particle sintering and thus obtain isolated nanoparticles. To do so, the temperature range between 750 and 850 °C could be explored in more detail. Lower temperatures should, in principle, lead to lower sintering between particles.

## EXPERIMENTAL SECTION

**Materials.** The metal salt precursors used for the synthesis of $CuFe_2O_4$ were iron nitrate [$Fe(NO_3)_3{\cdot}9H_2O$, Labkem] and copper nitrate [$Cu(NO_3)_2{\cdot}3H_2O$, Labkem], with poly(vinylpyrrolidone), PVP [$(C_6H_9NO)_n$, Sigma-Aldrich], as a gelling agent. Distilled water was used as the solvent.

**Design of Experiments, DoE.** The DoE approach is a powerful method used to optimize processes and quantitatively estimate the effect that different variables have in a process and their possible interactions. For this work, a Full Factorial Design ($2^K$) strategy was selected and two variables ($K = 2$) were analyzed: calcination temperature ($X_1$, in degrees) and time ($X_2$, in min). The evaluated response ($Y$, in percentage) was the purity of the obtained ferrite.

The upper and lower levels were defined in each of the two optimization cycles that were done in this work. Once the levels of variables were set, the experimental matrix was defined (see Table 8). As $K = 2$, the total number of experiments to be done was 4.

**Table 8. Experimental Matrix Definition**

| experiment # | $X_1$ | $X_2$ |
|---|---|---|
| 1 | − | − |
| 2 | + | − |
| 3 | − | + |
| 4 | + | + |

The "+" and "−" symbols represent, respectively, the upper and lower levels for each variable. Thus, a square design was planned, where corners of the four combinations were explored. With these conditions, the simple mathematical model described in eq 1 can be defined[28]

$$Y = b_0 + b_1X_1 + b_2X_2 + b_{12}X_1X_2 \quad (1)$$

where $Y$ is the response value (copper ferrite purity, in this case), $X_n$ corresponds to "+1" or "−1" values according to Table 8, and $b_n$ are experimentally deduced coefficients. Once the experimental values were obtained, it was possible to predict $Y$ at any point in the experimental domain.[28]

**Synthesis.** For the synthesis of $CuFe_2O_4$ nanoparticles by the polymer-assisted sol−gel method, a specific amount of PVP (ratio 1:1 with the aimed $CuFe_2O_4$ mass) was first dissolved in 200 mL of distilled water under stirring at room temperature for 2 h. Then, stoichiometric amounts of each nitrate precursor were added, and the solution was further stirred at room temperature for three additional hours. After this, the homogeneous solution was heated at 80 °C for 24 h in a furnace to dry the sample and polymerize the gelling agent. Thus, a solid gel containing a homogeneous distribution of the metal ions was obtained. To eliminate the organic matter and obtain the desired oxide, the gel was burned at 250 °C for 15 min in a furnace. The obtained product was further ground to powder, and finally, calcination was done to allow the ferrite formation. The calcination conditions are later specified for each sample, as these are the parameters optimized by the DoE.

**Characterization.** For each sample, chemical composition and crystal structure were determined by means of XRD measurements in a PANalytical X'Pert PRO MPD $\theta/\theta$ Bragg−Brentano powder diffractometer with a radius of 240 mm using Cu K$\alpha$ radiation ($\lambda$ = 1.5418 Å). Particle size measurement by LD was done using an LS 13 320MW from a Beckman Coulter device. To corroborate particle sizes, shape, and agglomeration, SEM images were obtained with a Field Emission SEM JEDL J-7100. Finally, magnetic properties were measured in a magnetometer SQUID Quantum Design MPMS XL.

## AUTHOR INFORMATION


### Corresponding Author

*E-mail: m.segarra@ub.edu.

### ORCID

Jaume Calvo-de la Rosa: 0000-0002-1624-2595


### Notes

The authors declare no competing financial interest.

## ACKNOWLEDGMENTS

J. Calvo-de la Rosa acknowledges Ajuts a la Docència i a la Recerca (ADR) given by the Universitat de Barcelona and the Catalan Government for the quality accreditation given to his research group DIOPMA (2017 SGR 118).

## REFERENCES


(1) Niemirowicz, K.; Markiewicz, K. H.; Wilczewska, A. Z.; Car, H. Magnetic Nanoparticles as New Diagnostic Tools in Medicine. *Adv. Med. Sci.* **2012**, *57*, 196−207.

(2) Gao, Y.; Lim, J.; Teoh, S.-H.; Xu, C. Emerging Translational Research on Magnetic Nanoparticles for Regenerative Medicine. *Chem. Soc. Rev.* **2015**, *44*, 6306−6329.

(3) Józefczak, A.; Kaczmarek, K.; Hornowski, T.; Kubovčíková, M.; Rozynek, Z.; Timko, M.; Skumiel, A. Magnetic Nanoparticles for Enhancing the Effectiveness of Ultrasonic Hyperthermia. *Appl. Phys. Lett.* **2016**, *108*, No. 263701.

(4) Shi, X.; Xiang, C.; Liu, Y.; Lin, H.; Xu, Y.; Ji, J. Preparation and Evaluation of Chitosan/$\beta$-Cyclodextrin Magnetic Nanoparticles as a Photodegradable and Hydrophobic Drug Delivery Carrier. *J. Appl. Polym. Sci.* **2017**, *134*, No. 45076.

(5) Kamzin, A. S.; Ranjith Kumar, E.; Ramadevi, P.; Selvakumar, C. The Properties of Mn−CuFe 2 O 4 Spinel Ferrite Nanoparticles under Various Synthesis Conditions. *Phys. Solid State* **2017**, *59*, 1841−1851.

(6) Chandra, S.; Patel, M. D.; Lang, H.; Bahadur, D. Dendrimer-Functionalized Magnetic Nanoparticles: A New Electrode Material for Electrochemical Energy Storage Devices. *J. Power Sources* **2015**, *280*, 217−226.

(7) Kovalenko, A.; Singh Yadav, R.; Pospisil, J.; Zmeskal, O.; Karashanova, D.; Heinrichová, P.; Vala, M.; Havlica, J.; Weiter, M. Towards Improved Efficiency of Bulk-Heterojunction Solar Cells Using Various Spinel Ferrite Magnetic Nanoparticles. *Org. Electron.* **2016**, *39*, 118−126.

(8) Galloway, J. M.; Talbot, J. E.; Critchley, K.; Miles, J. J.; Bramble, J. P. Developing Biotemplated Data Storage: Room Temperature




DOI: 10.1021/acsomega.9b02295
*ACS Omega* 2019, 4, 18289−18298

Biomineralization of L10 CoPt Magnetic Nanoparticles. *Adv. Funct. Mater.* **2015**, *25*, 4590−4600.
(9) Ohkoshi, S.i.; Namai, A.; Yoshikiyo, M.; Imoto, K.; Tamazaki, K.; Matsuno, K.; Inoue, O.; Ide, T.; Masada, K.; Goto, M.; et al. Multimetal-Substituted Epsilon-Iron Oxide $\epsilon$-Ga0.31TiO0.05-CoO0.05Fe1.59O3 for Next-Generation Magnetic Recording Tape in the Big-Data Era. *Angew. Chem., Int. Ed.* **2016**, *55*, 11403−11406.
(10) Salavati-Niasari, M.; Mahmoudi, T.; Sabet, M.; Hosseinpour-Mashkani, S. M.; Soofivand, F.; Tavakoli, F. Synthesis and Characterization of Copper Ferrite Nanocrystals via Coprecipitation. *J. Cluster Sci.* **2012**, *23*, 1003−1010.
(11) Kanagaraj, M.; Sathishkumar, P.; Selvan, G. K.; Kokila, P.; Arumugam, S. Structural and Magnetic Properties of CuFe 2 O 4 As-Prepared and Thermally Treated Spinel Nanoferrites. *Indian J. Pure Appl. Phys.* **2014**, *52*, 124−130.
(12) Moshtaghi, S.; Ghanbari, D.; Salavati-niasari, M. Characterization of CaSn (OH) 6 and CaSnO 3 Nanostructures Synthesized Bya New Precursor. *J. Nanostruct.* **2015**, *5*, 169−174.
(13) Sharifi, I.; Zamanian, A.; Behnamghader, A. Synthesis and Characterization of Fe0.6Zn0.4Fe2O4 Ferrite Magnetic Nanoclusters Using Simple Thermal Decomposition Method. *J. Magn. Magn. Mater.* **2016**, *412*, 107−113.
(14) Al-Gaashani, R.; Aïssa, B.; Anower Hossain, M.; Radiman, S. Catalyst-Free Synthesis of ZnO-CuO-ZnFe2O4 Nanocomposites by a Rapid One-Step Thermal Decomposition Approach. *Mater. Sci. Semicond. Process.* **2019**, *90*, 41−49.
(15) Lv, W.; Liu, B.; Luo, Z.; Ren, X.; Zhang, P. XRD Studies on the Nanosized Copper Ferrite Powders Synthesized by Sonochemical Method. *J. Alloys Compd.* **2008**, *465*, 261−264.
(16) Mir, N.; Salavati-Niasari, M.; Davar, F. Preparation of ZnO Nanoflowers and Zn Glycerolate Nanoplates Using Inorganic Precursors via a Convenient Rout and Application in Dye Sensitized Solar Cells. *Chem. Eng. J.* **2012**, *181−182*, 779−789.
(17) Gholami, T.; Salavati-Niasari, M.; Bazarganipour, M.; Noori, E. Synthesis and Characterization of Spherical Silica Nanoparticles by Modified Stöber Process Assisted by Organic Ligand. *Superlattices Microstruct.* **2013**, *61*, 33−41.
(18) Zinatloo-Ajabshir, S.; Salavati-Niasari, M. Facile Route to Synthesize Zirconium Dioxide (ZrO2) Nanostructures: Structural, Optical and Photocatalytic Studies. *J. Mol. Liq.* **2016**, *216*, 545−551.
(19) Kalam, A.; Al-Sehemi, A. G.; Assiri, M.; Du, G.; Ahmad, T.; Ahmad, I.; Pannipara, M. Modified Solvothermal Synthesis of Cobalt Ferrite (CoFe 2 O 4) Magnetic Nanoparticles Photocatalysts for Degradation of Methylene Blue with H 2 O 2 /Visible Light. *Results Phys.* **2018**, *8*, 1046−1053.
(20) Kurian, J.; Mathew, M. J. Structural, Optical and Magnetic Studies of CuFe2O4, MgFe2O4 and ZnFe2O4 Nanoparticles Prepared by Hydrothermal/Solvothermal Method. *J. Magn. Magn. Mater.* **2018**, *451*, 121−130.
(21) Zakiyah, L. B.; Saion, E.; Al-Hada, N. M.; Gharibshahi, E.; Salem, A.; Soltani, N.; Gene, S. Up-Scalable Synthesis of Size-Controlled Copper Ferrite Nanocrystals by Thermal Treatment Method. *Mater. Sci. Semicond. Process.* **2015**, *40*, 564−569.
(22) López-Ramón, M. V.; Álvarez, M. A.; Moreno-Castilla, C.; Fontecha-Cámara, M. A.; Yebra-Rodríguez, Á.; Bailón-García, E. Effect of Calcination Temperature of a Copper Ferrite Synthesized by a Sol-Gel Method on Its Structural Characteristics and Performance as Fenton Catalyst to Remove Gallic Acid from Water. *J. Colloid Interface Sci.* **2018**, *511*, 193−202.
(23) Zhuravlev, V. A.; Minin, R. V.; Itin, V. I.; Lilenko, I. Y. Structural Parameters and Magnetic Properties of Copper Ferrite Nanopowders Obtained by the Sol-Gel Combustion. *J. Alloys Compd.* **2017**, *692*, 705−712.
(24) Satheeshkumar, M. K.; Ranjith Kumar, E.; Srinivas, C.; Prasad, G.; Meena, S. S.; Pradeep, I.; Suriyanarayanan, N.; Sastry, D. L. Structural and Magnetic Properties of CuFe 2 O 4 Ferrite Nanoparticles Synthesized by Cow Urine Assisted Combustion Method. *J. Magn. Magn. Mater.* **2019**, *484*, 120−125.
(25) Satheeshkumar, M. K.; Ranjith Kumar, E.; Srinivas, C.; Suriyanarayanan, N.; Deepty, M.; Prajapat, C. L.; Rao, T. V. C.; Sastry, D. L. Study of Structural, Morphological and Magnetic Properties of Ag Substituted Cobalt Ferrite Nanoparticles Prepared by Honey Assisted Combustion Method and Evaluation of Their Antibacterial Activity. *J. Magn. Magn. Mater.* **2019**, *469*, 691−697.
(26) Zinatloo-Ajabshir, S.; Morassaei, M. S.; Salavati-Niasari, M. Facile Fabrication of Dy2Sn2O7-SnO2 Nanocomposites as an Effective Photocatalyst for Degradation and Removal of Organic Contaminants. *J. Colloid Interface Sci.* **2017**, *497*, 298−308.
(27) Masunga, N.; Kelebogile Mmelesi, O.; Kefeni, K. K.; Mamba, B. B. Recent Advances in Copper Ferrite Nanoparticles and Nanocomposites Synthesis, Magnetic Properties and Application in Water Treatment: Review. *J. Environ. Chem. Eng.* **2019**, *7*, No. 103179.
(28) Leardi, R. Experimental Design in Chemistry: A Tutorial. *Anal. Chim. Acta* **2009**, *652*, 161−172.
(29) Mahapatra, C.; Kim, H.-W.; Alqaysi, M.; Han, C.-M.; Singh, R. K.; Owens, G. J.; Foroutan, F.; Knowles, J. C. Sol−Gel Based Materials for Biomedical Applications. *Prog. Mater. Sci.* **2016**, *77*, 1−79.
(30) Khemthong, P.; Kongmark, C.; Kochaputi, N.; Mahakot, S.; Rodporn, S.; Faungnawakij, K. In Situ X-Ray Absorption Fine Structure Probing-Phase Evolution of CuFe2O4 in Nanospace Confinement. *Inorg. Chem.* **2019**, *58*, 6584−6587.
(31) Esteve, V. *El Método de Rietveld*; Universitat Jaume I: Castelló de la Plana, 2006.
(32) Sumangala, T. P.; Mahender, C.; Barnabe, A.; Venkataramani, N.; Prasad, S. Structural, Magnetic and Gas Sensing Properties of Nanosized Copper Ferrite Powder Synthesized by Sol Gel Combustion Technique. *J. Magn. Magn. Mater.* **2016**, *418*, 48−53.
(33) Anandan, S.; Selvamani, T.; Prasad, G. G.; M. Asiri, A.; J. Wu, J. Magnetic and Catalytic Properties of Inverse Spinel CuFe 2 O 4 Nanoparticles. *J. Magn. Magn. Mater.* **2017**, *432*, 437−443.
(34) Yadav, R. S.; Havlica, J.; Masilko, J.; Kalina, L.; Wasserbauer, J.; Hajdúchová, M.; Enev, V.; Kuřitka, I.; Kožáková, Z. Cation Migration-Induced Crystal Phase Transformation in Copper Ferrite Nanoparticles and Their Magnetic Property. *J. Supercond. Novel Magn.* **2016**, *29*, 759−769.



DOI: 10.1021/acsomega.9b02295
*ACS Omega* 2019, 4, 18289−18298